A Lyα Transit Left Undetected: the Environment and Atmospheric Behavior of K2-25b

Keighley E. Rockcliffe[1] , Elisabeth R. Newton[1] , Allison Youngblood[2] , Vincent Bourrier[3] , Andrew W. Mann[4] ,
Zachory Berta-Thompson[5] , Marcel A. Agüeros[6] , Alejandro Núñez[6] , and David Charbonneau[7]

[1] Department of Physics and Astronomy, Dartmouth College, Hanover, NH 03755, USA
[2] Laboratory for Atmospheric and Space Physics, University of Colorado Boulder, Boulder, CO 80303, USA
[3] Observatoire Astronomique de l'Université de Genève, Chemin Pegasi 51b, CH-1290 Versoix, Switzerland
[4] Department of Physics and Astronomy, University of North Carolina at Chapel Hill, Chapel Hill, NC 27599, USA
[5] Department of Astrophysical & Planetary Sciences, University of Colorado Boulder, Boulder, CO 80303, USA
[6] Department of Astronomy, Columbia University, New York, NY 10027, USA
[7] Center for Astrophysics—Harvard-Smithsonian, Cambridge, MA 02139, USA

Abstract

K2-25b is a Neptune-sized exoplanet ($3.45 R_\oplus$) that orbits its M4.5 host with a period of 3.48 days. Due to its membership in the Hyades Cluster, the system has a known age (727 ± 75 Myr). K2-25b's youth and its similarities with Gl 436b suggested that K2-25b could be undergoing strong atmospheric escape. We observed two transits of K2-25b at Lyα using HST/STIS in order to search for escaping neutral hydrogen. We were unable to detect an exospheric signature, but placed an upper limit of $(R_p/R_\star)|_{Ly\alpha} < 0.56$ at 95% confidence by fitting the light curve of the Lyα red wing, or < 1.20 in the blue wing. We reconstructed the intrinsic Lyα profile of K2-25 to determine its Lyα flux, and analyzed XMM-Newton observations to determined its X-ray flux. Based on the total X-ray and extreme ultraviolet irradiation of the planet (8763 ± 1049 erg s^{-1} cm^{-2}), we estimated the maximum energy-limited mass-loss rate of K2-25b to be $10.6^{+15.2}_{-6.13} \times 10^{10}$ g s^{-1} ($0.56 M_\oplus$ per 1 Gyr), five times larger than the similarly estimated mass-loss rate of Gl 436b (2.2×10^{10} g s^{-1}). The photoionization time is about 3 hr, significantly shorter than Gl 436b's 14 hr. A nondetection of a Lyα transit could suggest K2-25b is not significantly losing its atmosphere, or factors of the system are resulting in the mass loss being unobservable (e.g., atmosphere composition or the system's large high-energy flux). Further observations could provide more stringent constraints.

Unified Astronomy Thesaurus concepts: Exoplanets (498); Hot Neptunes (754)

1. Introduction

Features in the exoplanet radius–period diagram are consequences of exoplanetary formation and evolutionary processes. In particular, the "hot-Neptune desert" and the "radius gap" motivate understanding atmospheric escape. The hot-Neptune desert is the lack of short-period planets ($P_p \lesssim 3$ days) with radii between that of super-Earths and Jupiter (Lecavelier Des Etangs 2007; Davis & Wheatley 2009; Szabó & Kiss 2011; Beaugé & Nesvorný 2013; Kurokawa & Nakamoto 2014; Lundkvist et al. 2016; Mazeh et al. 2016). Atmospheric escape, along with orbital migration, is one of the dominant processes thought to shape the desert (Mazeh et al. 2016; Owen & Lai 2018). The second feature, the radius gap, is the gap in the distribution of planetary radii around $1.5 - 2 R_\oplus$ (Owen & Wu 2013; Fulton et al. 2017; Fulton & Petigura 2018). The radius gap can also be attributable to atmospheric escape (Lopez & Fortney 2013; Owen & Wu 2013; Jin et al. 2014; Ginzburg et al. 2018), though Lee & Connors (2021) argue it can be primordial.

Atmospheric escape occurs on every planet with an atmosphere, but may have more or less influence on a its evolution depending on the planetary properties (e.g., bulk density, atmospheric composition, magnetic field) and environment (e.g., irradiation, stellar wind, impact erosion). The two atmospheric escape processes that have been mostly explored as shapers of the exoplanet population are thermal irradiation-driven (photo evaporation) and core-cooling-driven (core-powered mass-loss) processes.

Photo evaporation occurs when a close-in planet with a volatile-dominated atmosphere receives a large flux of high-energy radiation from its host. The radiation heats the planet's upper atmosphere leading to the bulk motion of particles outward in a hydrodynamic outflow (see Owen 2019 for a review). It follows that the timescale for this process is closely tied to the evolution of the star's high-energy radiation. Although a timescale of 100 Myr is commonly accepted as it traces the period of highest stellar X-ray output (e.g., Lopez & Fortney 2013; Owen & Wu 2017), King & Wheatley (2021) discuss the possibility of a longer Gyr timescale following the slower decline in extreme ultraviolet (EUV) output. Alternatively, Ginzburg et al. (2018) found that the luminosity from a cooling exoplanetary core (core-powered mass loss) can heat the atmosphere from below and cause hydrodynamic outflow. Exploring atmospheric escape within a range of host spectral types can distinguish between photo evaporation and core-powered mass loss (e.g., Ginzburg et al. 2018). These two processes have different dependencies on stellar and planetary properties, and different timescales for evolution.

One of the most important tracers of atmospheric escape is the Lyα emission line (Lyα; 1215.672 Å). A host star's Lyα radiation readily interacts with neutral hydrogen in the planetary atmosphere. While interstellar hydrogen usually completely absorbs Lyα at the emission line center, a planet transit can be observed at Lyα if the planetary hydrogen atoms are accelerated to high velocities such that they attenuate the wings of the line profile. The exact acceleration mechanisms remain an open question in the community. Atmospheric modeling work suggests that radiation pressure and stellar wind interactions change the spectral signature of the exosphere (Holmström et al. 2008; Ben-Jaffel & Sona Hosseini 2010; Tremblin & Chiang 2013; Bourrier et al. 2015, 2016, 2018a;

Table 1
K2-25 System Properties

Properties (Symbol)	Value	Units
Earth-system distance (d)	45.014 ± 0.165	pc
Age (τ)[a]	727 ± 75	Myr
Right ascension (α)	04:13:05.62	hh:mm:ss
decl. (δ)	+15:14:51.9	dd:mm:ss
Spectral type	M4.5	
Bolometric luminosity (L_{bol})	$8.16 \pm 0.29 \times 10^{-3}$	$L_\odot$
Stellar mass ($M_\star$)	0.2634 ± 0.0077	$M_\odot$
Stellar radius ($R_\star$)	0.2932 ± 0.0093	$R_\odot$
Stellar rotation period ($P_\star$)	1.88 ± 0.02	days
Barycentric radial velocity ($v_\star$)	38.64 ± 0.15	km s^{-1}
Epoch (t_0)	2457062.57965 ± 0.0002	BJD
Transit duration	$0.79^{+0.09}_{-0.17}$	days
Planetary mass estimate[b] (M_p)	7^{+10}_{-4}	$M_\oplus$
Planetary mass measurement[c]	$24.5^{+5.7}_{-5.2}$	$M_\oplus$
Planetary radius (R_p)	$3.4492^{+0.1099}_{-0.1110}$	$R_\oplus$
Orbital period (P_p)	$3.48456322^{+9.7\times10^{-7}}_{-9.5\times10^{-7}}$	days
Semimajor axis (a)	0.0288 ± 0.0003	au

Notes. Parameters are from Mann et al. (2016) and Thao et al. (2020).
[a] Age estimate of the Hyades cluster as determined by Douglas et al. (2019).
[b] Mass estimate from Kain et al. (2020) using the mass–radius relation implemented in MRExo (Ning et al. 2018; Kanodia et al. 2019).
[c] Mass measurement from Habitable Zone Planet Finder radial velocity observations (Stefansson et al. 2020b).

Villarreal D'Angelo et al. 2018; McCann et al. 2019; Debrecht et al. 2020).

Neutral hydrogen exospheres in two transiting hot Neptunes, Gl 436b (sometimes referred to as GJ 436b; dos Santos et al. 2019; Lavie et al. 2017; Ehrenreich et al. 2015; Kulow et al. 2014) and GJ 3470b (Bourrier et al. 2018a), have been detected. These planets orbit their M-dwarf hosts within 0.03 au and are therefore subject to high radiation levels. Observations with the Hubble Space Telescope (HST) Space Telescope Imaging Spectrograph (STIS) and the Cosmic Origins Spectrograph show deep and temporally asymmetric Lyα attenuation surrounding the white-light transit. These data suggest an extended comet-like hydrogen tail surrounding the planets.

K2-25b is a Neptune-sized short-period exoplanet within the 727 ± 75 Myr-old Hyades cluster (Gossage et al. 2018) that was discovered using photometry from the K2 mission (Mann et al. 2016). K2-25b orbits around its young M4.5V host with a period of 3.48 days. We review the physical properties of the K2-25 system in Table 1, and compare K2-25b to the Neptune-sized planets with detected neutral hydrogen exospheres in Figure 1.

Determining how system properties like planetary atmospheric composition and youth impact mass loss is an important part of understanding atmospheric escape. Young exoplanets are particularly important for this study because they experience extreme stellar environments and directly probe the theorized ∼100 Myr timescale for photo evaporation. Constraining the mass-loss rate and timescale for photo evaporation in young planets will test and improve exoplanet demographic studies. This motivates a detailed study of K2-25b and its radiation environment. Gaidos et al. (2020) previously analyzed infrared transmission spectra for K2-25b and did not detect escaping helium; here, we consider neutral hydrogen escape. We obtained HST/STIS Lyα observations of
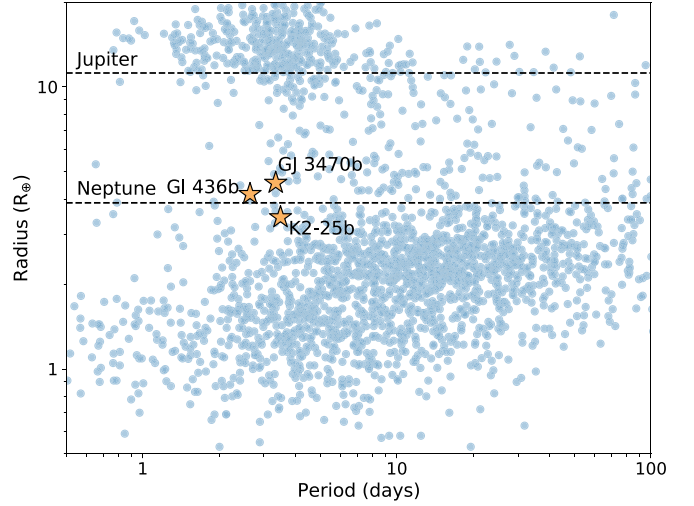
Figure 1. The distribution of radii (in Earth radii) as a function of orbital period (in days) for exoplanets within the NASA Exoplanet Archive as of March 2021.

K2-25b (HST-GO-14615; PI: Newton), which we present in Section 2. Analysis of the Lyα light curves is presented in Section 3. We measure the Lyα and X-ray flux of K2-25, and estimate the energy-limited mass-loss rate for K2-25b in Section 4. We conclude by discussing the implications of our results in Section 5.

2. Lyα Line Observations and Analysis

We observed K2-25 with the 52 x 0.″1 aperture using HST's STIS. We used the G140M grating with a spectral range of 1140–1741 Å and a resolving power of ∼10,000. We observed with the far-ultraviolet multianode microchannel array in TIME-TAG mode. Two HST visits occurred on 2017 March 23 (Visit 1) and 2017 October 31 (Visit 2), each corresponding to a transit of K2-25b. Eight science exposures were taken for each visit, each spanning the observable window of an HST orbit (about 2000 s). TIME-TAG mode observations individually stamp the arrival time for each photon detected by the instrument. These time stamps allowed us to split the full exposures, prior to extraction and reduction, into three subexposures of 684 s or 625 s each.

We used the calstis pipeline (v3.4) to reduce these data. We automatically located the extraction apertures by determining the centroid of the Lyα red wing. We used the calstis pipeline to extract the background in two regions 15 pixels above and below the extraction location. We used these extraction regions to fit the spatial direction with the default third-order polynomial, and this fit was used to remove the background from the target spectrum. We did not find the choice of polynomial order to be important. Cycle 27 calibration files were used to assign wavelengths to each pixel and then convert flux in counts to specific flux values (erg s^{-1} cm^{-2} Å^{-1}).

Errors from calstis are based on $\sqrt{N}$, which is inaccurate for small N (the total counts). Equation (1) approximates the confidence limit for a Poisson distribution, corresponding to a Gaussian 1σ limit (Gehrels 1986). We used Equation (1) to recalculate errors for our spectra from the total counts (the
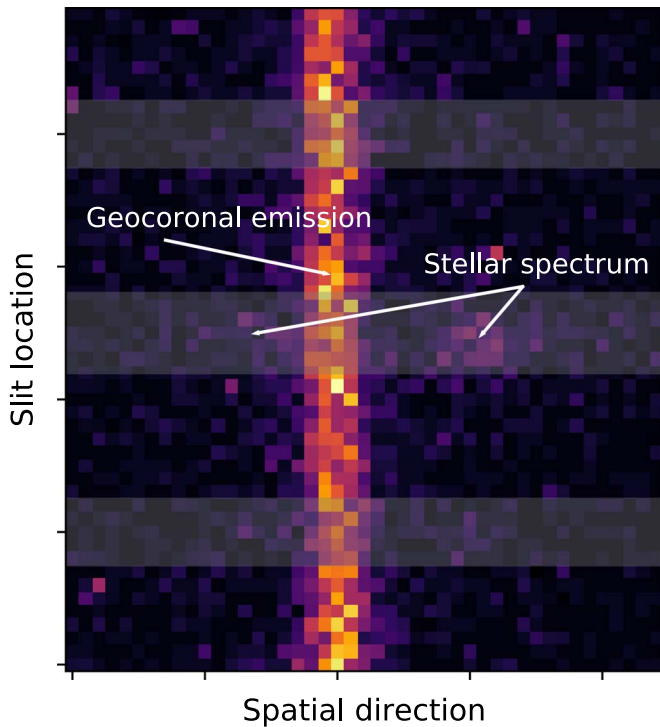
Figure 2. An example of the two-dimensional raw data taken by *HST*/STIS during a full orbit within Visit 1. The spectral trace and the two background locations are highlighted in gray. In Visit 1, the geocoronal emission encroaches on the blue wing of the Lyα line.

GROSS spectrum in the `calstis` data products):

$$\sigma \approx 1 - \sqrt{N + 0.75}. \qquad (1)$$

The error at each pixel was then converted to flux units using the flux conversion factors we inferred from the `calstis` data products.

We looked for the HST "breathing effect" (thermal changes in the telescope optics and focal plane), which can cause variability in flux throughput over the course of an HST orbit (Bowers 1997; Brown et al. 2001; Sing et al. 2008; Huitson et al. 2012; Bourrier et al. 2013). We created six light curves for the Lyα line (three per visit) by grouping consecutive spectra. We folded the light curves on HST's orbital period, and fit a sloped line to the flux as a function of orbital phase for each one. We also looked at the behavior of each exposure individually. In all cases, a sloped line fit and a horizontal line fit were similar as shown by their Bayesian Information Criteria ($|\text{BIC}_{\text{slope}} - \text{BIC}_{\text{flat}}| \sim 2$), so we did not include a systematics correction in our analysis.

The raw data are contaminated with geocoronal airglow from solar Lyα photons scattered off of the Earth's atmosphere (Figure 2). Though largely removed by background subtraction, contaminated regions should be treated with caution, as evidenced by the increased scatter in these regions as seen in Figure 3 (gray regions). The contamination is of particular concern in Visit 1 because the geocoronal emission coincides with the blue wing of K2-25's Lyα profile.

Given K2-25's systemic velocity, the Lyα line center is not observable at Earth due to the high neutral hydrogen column density, and for this reason we consider the Lyα wings. The individual spectra in the two panels of Figure 3 temporally resolve each transit. If significant exospheric neutral hydrogen

was present at high enough speeds, the wing of the Lyα profile would be attenuated during the exosphere transit. For comparison, one observation of the warm Neptune Gl 436b yielded a 56.2% transit in the blue wing of Lyα starting 2 hr before and ending between 10 and 25 hr after the optical transit time of the planet (Lavie et al. 2017). No deep transit is obvious for K2-25b during either Visit 1 or 2 (see Figure 3); all spectra taken during and outside of the planet transit are visually consistent.

3. K2-25's Light Curve

We created two Lyα light curves from our observations, one for the Lyα blue wing and the other for the red wing, in order to quantitatively investigate the presence of a transit. Our analysis uses the subexposures obtained from the TIME-TAG mode data. To obtain fluxes at each point in time, we summed over the stellar reference frame velocities -165.2 to -29.5 km s^{-1} for the blue wing, and 44.3 to 229.3 km s^{-1} for the red wing (Figure 4).

We normalized all of the subexposure fluxes to the out-of-transit data using a linear fit to the full exposure data points that are beyond ± 5 hr of midtransit. Both visits were combined into a single light curve as a function of planetary orbital phase (time from midtransit). With sufficient signal and cadence, light curves such as these can constrain the radius and characterize the behavior of the potentially escaping neutral hydrogen.

We compared the Lyα red-wing light curve to K2-25's N V emission to look for evidence of non-transit-related variability (e.g., flares). M-dwarf flares enhance N V flux more than Lyα and therefore should be more indicative of activity influencing our light curves (Loyd et al. 2018). Two potential flares in N V were indicated in Gaidos et al. (2020); improved error analysis does not support the presence of significant variability. Inclusion of the two points discarded in Gaidos et al. (2020) does not impact the results of that work. Since no flaring was evident in N V or Lyα we used all data in our analysis.

We assumed the exosphere can be represented by a transiting opaque disk, and model the light curves with BATMAN (Kreidberg 2015). The S/N of our data does not warrant considering more complicated transit shapes (e.g., asymmetry). While Gl 436b does produce a clear asymmetric transit shape, GJ 3470b's transit is relatively symmetric (see Figures 2 and 5 in Bourrier et al. 2016, 2018a). The full BATMAN transit model consists of eight parameters: the midtransit time (t_0), period (P_p), ratio of the planetary radius to stellar radius ($R_p/R_\star$), semimajor axis (a), inclination (i), eccentricity (e), argument of periastron (ω), and the limb-darkening coefficients (u). We only fit for the transit depth, fixing all other parameters to the values listed in Table 2. The limb-darkening coefficients were assumed to be 0, but are irrelevant given the sparse sampling of our data.

There is a dip in the flux of both wings at ~ 1 hr after the fixed transit time, lasting for one orbit. At this time, we do not explore asymmetric transits. Instead, we fit the same transit model, but vary the midtransit time. The best-fit results in a transit in both the blue and red wings are centered at ~ 1 hr, which does not overlap with the transit ephemeris (the errors on the transit ephemeris are fractions of a minute, and Kain et al. (2020) found no evidence of transit timing variations). As we are not aware of a model that would produce a signal like this,
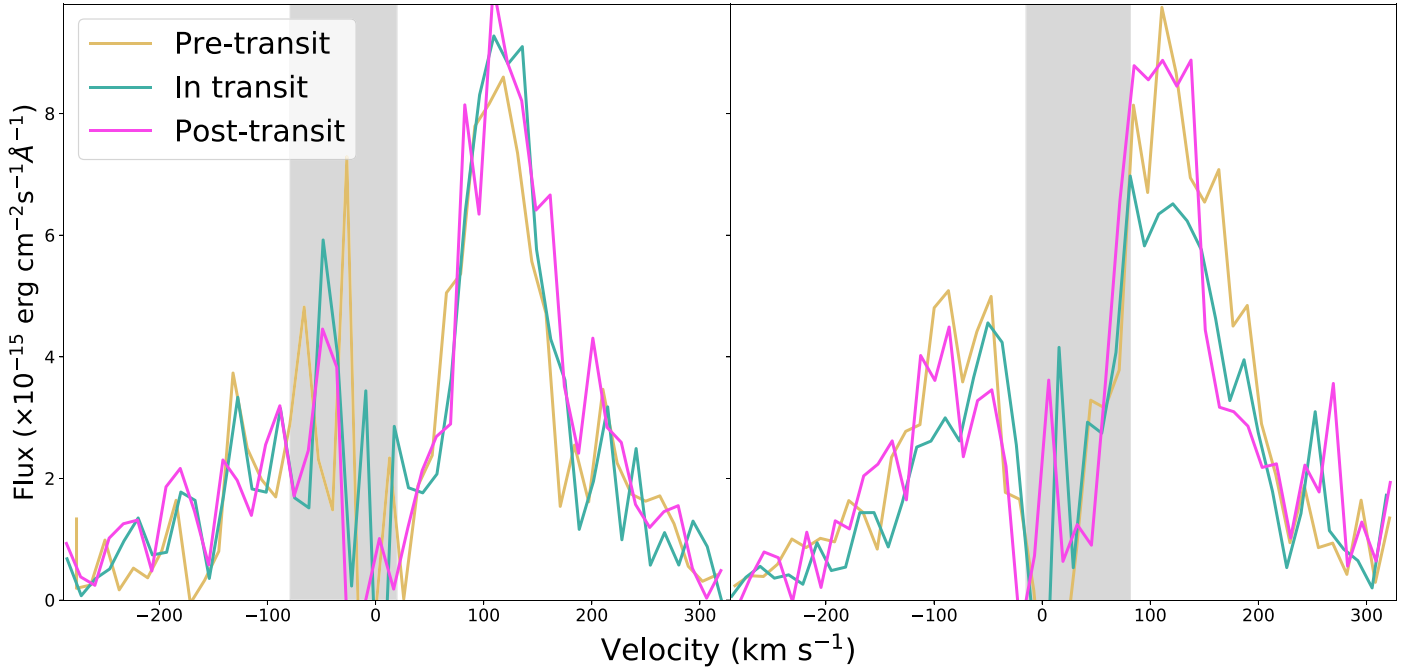
Figure 3. The spectra of K2-25 during Visits 1 (left) and 2 (right). The different colors indicate the average spectrum prior to transit (yellow), at times near the white-light transit (green), and after the transit (pink). The gray shaded region indicates the location of the geocoronal emission region that was removed from the spectra. Velocities are in the host star's reference frame.
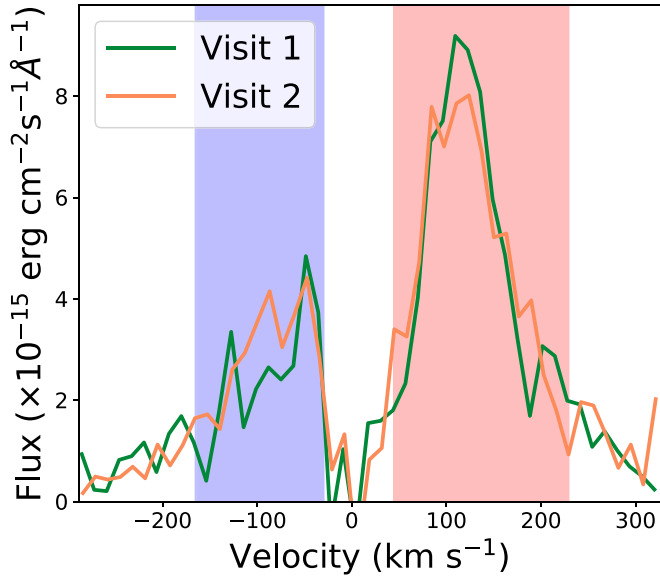
Figure 4. The Lyα average profiles for Visits 1 and 2. The integrated regions of the blue and red wing are shaded in blue and red, respectively. Velocities are in the host star's reference frame. The two average spectra are included as the Data behind the Figure in a .tar.gz package. The 48 TIME-TAG spectra (24 per *HST* visit) are also included.

Table 2
Light-curve Parameters

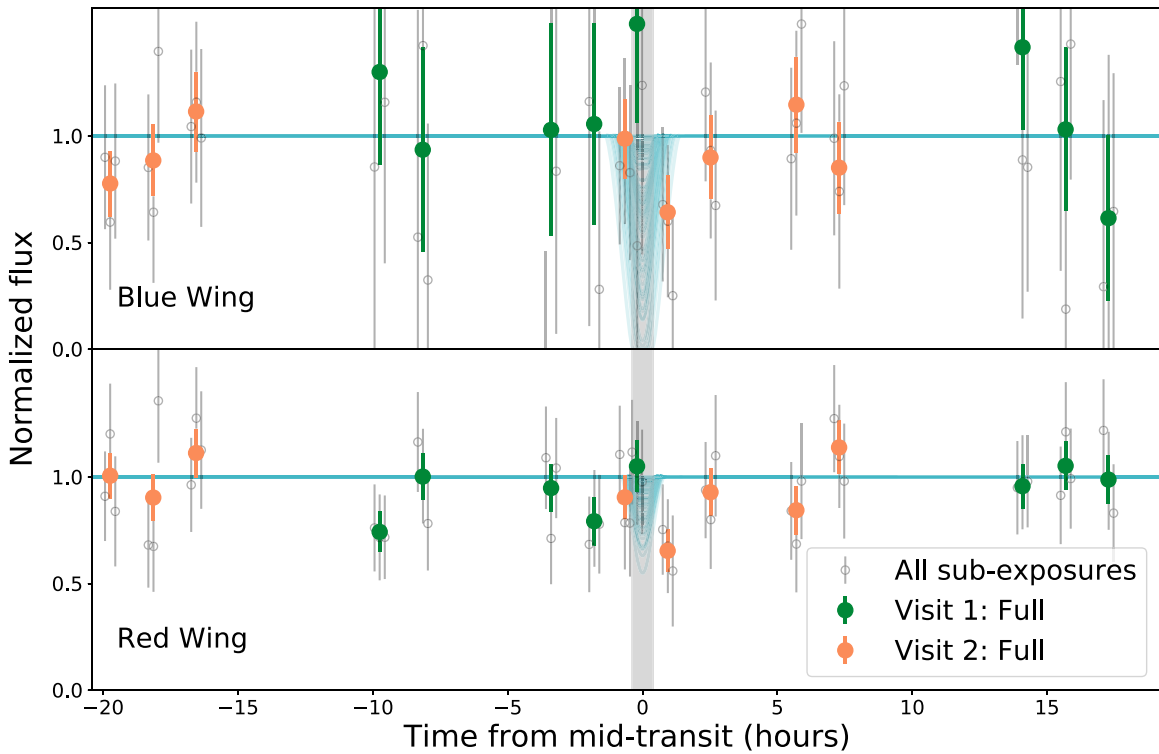| Parameter	Value	Units
t_0 [a]	0	hr
$P_{\rm p}$	3.48456322	days
a	0.0288	AU
i	88.164	degrees
e	0.27	
w	98.0	degrees

Note.
[a] The uncertainties on each transit epoch where we obtained observations are fractions of a minute, which allows us to fix this value.

4. K2-25's High-energy Environment

Photo evaporation in the energy-limited regime is controlled by the entire X-ray to extreme ultraviolet (XUV) spectrum (5–1170 Å, Lammer et al. 2003; Yelle 2004; Murray-Clay et al. 2009; Owen & Jackson 2012). To investigate K2-25b's radiation environment, we determine the star's Lyα, EUV, and X-ray flux. We then use these results to estimate the energy-limited mass-loss and photoionization rates for K2-25b.

4.1. The Intrinsic Lyα Line

We reconstructed the host's Lyα emission, modeling the intrinsic Lyα profile and the attenuation from the interstellar medium (ISM). We based our reconstruction on the combined spectrum from all HST orbits because there was no planetary signal in the data. To produce the combined spectrum, we performed a weighted average of all 16 spectra. We weighted the spectra by the associated error, using an average "error spectrum" for the two visits, which was applied to all eight spectra from that visit. We used this method to avoid biasing fluxes to lower values. While the error bars for the spectra from

we assume this dip is not indicative of an exosphere and fix the midtransit time to that expected from the white-light transit.

The ratio of the planetary radius to the stellar radius was left to vary with a uniform prior and a lower limit of 0. We fit the model to the red and blue light curves using the Markov Chain Monte Carlo algorithm `emcee` (Foreman-Mackey et al. 2013). Figure 5 shows the blue and red wing Lyα light curves and samples from the posterior distribution. The upper limits on $R_p/R_\star$ for the blue and red wing light curves are, respectively, 1.20 and 0.56 at 95% confidence.

Figure 5. Light curves for Lyα's blue wing (top) and red wing (bottom). Each panel has 16 filled circles, representing all of the full exposures from Visits 1 (green) and 2 (orange). The 48 empty circles are the subexposures. Samples from the posterior distributions are shown as light blue lines. The white-light transit time is shown by the gray shaded region.

within each visit are consistent with each other, the changing location of the geocoronal emission means the errors changes between the two visits (see Figure 3). We compute the average error spectrum by averaging the errors at each pixel for the eight spectra from a single visit.

We used the model developed in Youngblood et al. (2016) that describes the transmission profile of a local low-mass star with nine parameters. The model and fitting algorithm are available in the Python package `lyapy`.[8]

The emission profile was composed of a narrow and broad Gaussian, each characterized by an amplitude (A_n and A_b), full width half maximum (FW$_n$ and FW$_b$), and heliocentric velocity centroid (v_n and v_b). The interstellar medium attenuation was modeled with a Voigt profile approximation (Harris 1948) described by a Doppler broadening parameter (b), line-of-sight H I column density ($N_{\rm H\,I}$), and velocity centroid ($v_{\rm H\,I}$). The interstellar medium's D I content was characterized by the D/H ratio, which was left to vary. The velocity centroid for deuterium absorption was assumed to be the same as neutral hydrogen.

This model assumes that all of the interstellar neutral hydrogen exists in one cloud. While the LISM Dynamical Model (Redfield & Linsky 2008) outputs three clouds in the direction of K2-25, the low S/N of our spectra are not sufficient to constrain multiple ISM components (Youngblood et al. 2016).

We fit the stellar emission and ISM attenuation to the observed Lyα spectrum ($-350 < v < 390$ km s^{-1}). `lyapy` uses the MCMC sampler (`emcee`; Foreman-Mackey et al. 2013) to explore the parameter space. The chains were initialized by randomly sampling a normal distribution. The Doppler broadening parameter had a logarithmic prior. Uniform priors were assumed for all other varied parameters, including the column density ($N_{\rm H\,I}$). The posterior

distributions were sampled 100,000 times with a burn-in of 20,000 for 30 walkers.

We took the median of each one-dimensional posterior distribution (marginalized distribution) as the best-fit value and defined the uncertainty by the 16th and 84th percentiles of the distribution. The best-fit values and their uncertainties are listed in Table 3. The best-fit column density, $\log_{10} N_{\rm H\,I} = 18.14^{+0.08}_{-0.08}$, is consistent with the column density obtained by the Colorado Model of the Local Interstellar Cloud (Redfield & Linsky 2000) for the line of sight to K2-25, $\log_{10} N_{\rm H\,I} = 18.17$. There are two other clouds (Hyades, Aur) that are predicted to lie along K2-25's sight line (Redfield & Linsky 2008), which could account for the differences between our ISM results and the literature. The best-fit deuterium-to-hydrogen ratio (D/H = $6.95^{+6.40}_{-4.37} \times 10^{-6}$) has large enough uncertainties such that it is consistent with the accepted literature value of 1.5×10^{-5} found by Linsky et al. (2006; see also Hébrard & Moos 2003; Wood et al. 2004). The large uncertainties in the flux within the profile region where deuterium absorption occurs (~ -100 to -40 km s^{-1}) result from the overlap with the geocoronal emission region in Visit 1 (see Figure 3).

K2-25's reconstructed Lyα profile is shown in Figure 6. K2-25's Lyα flux at 1 au from the star is $1.38^{+0.18}_{-0.13}$ erg s^{-1} cm^{-2}, where the uncertainties are 1σ error bars.

4.2. The EUV Spectrum

We estimated K2-25's EUV spectrum (100–1170 Å) using empirical relations from Linsky et al. (2014). Using updated solar upper atmospheric models from Fontenla et al. (2014); Linsky et al. (2014) determined that the relationship between EUV and Lyα flux is roughly constant with Lyα flux. They obtained EUV to Lyα flux ratios in nine wave bands from

_____

Table 3
The Best-fit Parameter Values with 1σ Uncertainties for the Intrinsic Lyα Profile

Parameter	Value	Units	Description
v_n	$38.19^{+2.70}_{-2.17}$	km s^{-1}	narrow component velocity centroid
$\log_{10}A_n$	$-13.75^{+0.08}_{-0.07}$	erg s^{-1} cm^{-2} Å^{-1}	narrow component amplitude
FW$_n$	$163.40^{+15.64}_{-16.27}$	km s^{-1}	narrow component FWHM
v_b	$38.56^{+2.87}_{-2.45}$	km s^{-1}	broad component velocity centroid
$\log_{10}A_b$	$-14.72^{+0.21}_{-0.26}$	erg s^{-1} cm^{-2} Å^{-1}	broad component amplitude
FW$_b$	$447.17^{+178.28}_{-78.07}$	km s^{-1}	broad component FWHM
$\log_{10}N_{\mathrm{H\,I}}$	$18.14^{+0.08}_{-0.08}$		ISM H I column density
b	$8.62^{+3.22}_{-4.01}$	km s^{-1}	ISM Doppler broadening parameter
$v_{\mathrm{H\,I}}$	$12.91^{+2.83}_{-2.80}$	km s^{-1}	ISM velocity centroid
D/H	$6.95^{+6.40}_{-4.37} \times 10^{-6}$		ISM deuterium-to-hydrogen ratio
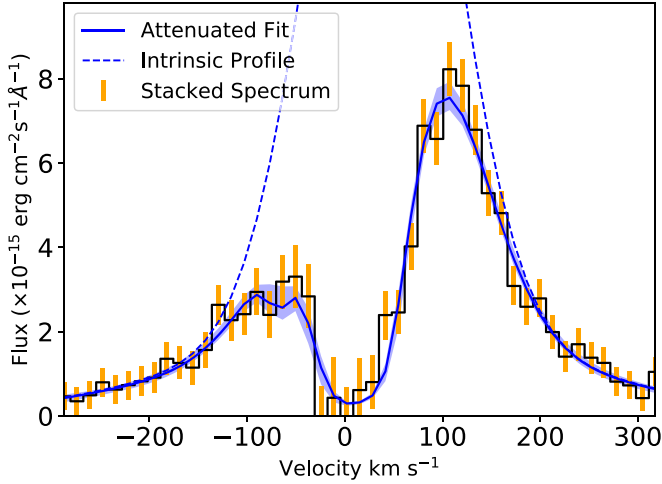
Figure 6. Our reconstructed Lyα profile for K2-25 (dashed blue). The spectrum created from the sixteen stacked exposures is included in black, with errors in orange. The best-fit profile—a combination of the Lyα double component Gaussian profile and the ISM's attenuating Voigt profile—is depicted as the solid blue line with 1σ errors shown in shaded blue.

100–1170 Å (indicated in Table 4). These relations are accurate within 20%, as inferred from the spectra of F5 V—M5 V stars observed with the Extreme UltraViolet Explorer and *Far Ultraviolet Spectroscopic Explorer* (Linsky et al. 2014). Each wave band was summed and scaled to calculate the total EUV flux of K2-25 at 1 au, 1.40 ± 0.14 erg s^{-1} cm^{-2}.

There may be additional, unaccounted for, systematic errors in the EUV spectrum for K2-25 because stars of its mass and age have not been thoroughly investigated by the models and observations. For example, Peacock et al. (2019) showed that the EUV fluxes for Gl 436 from synthetic spectra and from the relations within Linsky et al. (2014) can differ by a factor of a few.

4.3. The X-ray Spectrum

K2-25 was observed with XMM-Newton for a broad investigation into stellar rotation and activity (OBSID 0782061001; PI: Agüeros). The spectrum covers 5–100 Å (0.12–2.48 keV). We fit the spectrum output from the XMM-Newton/MOS1 instrument with a one-temperature VAPEC model, which characterizes the emission associated with collisionally-ionized gas (e.g., stellar coronae). The fit was performed with the HEASARC software xspec,[9] an X-ray spectral fitting package. The fitted spectrum

---

[9] https://heasarc.gsfc.nasa.gov/xanadu/xspec/

Table 4
K2-25's X-ray and EUV Emission

Wave band (Å)	Flux at 1 au (erg s^{-1} cm^{-2})	Uncertainty (erg s^{-1} cm^{-2})
5–100	5.883	$+1.159/-0.563$
100–200	0.444	±0.089
200–300	0.389	±0.079
300–400	0.344	±0.069
400–500	0.008	±0.002
500–600	0.013	±0.003
600–700	0.018	±0.004
700–800	0.021	±0.004
800–912	0.027	±0.005
912–1170	0.139	±0.028
Lyα	1.375	$+0.182/-0.126$

was integrated to get a total soft X-ray flux with 1σ uncertainty of $5.88^{+1.16}_{-0.56}$ erg s^{-1} cm^{-2} at 1 au from the star. The ratio of K2-25's X-ray luminosity to its bolometric luminosity is $\log_{10}L_X/L_{\mathrm{bol}} = -3.28$.

K2-25's Rossby number, defined as the ratio of the rotation period to its convective turnover time, is 0.02 according to the mass-convective turnover time relation from Wright et al. (2018). Its Rossby number places K2-25 in the saturated part of the rotation-coronal activity relation, where the X-ray emission appears to decouple from a star's rotation rate and is roughly constant. For 20 Hyades members with $M_* < 1.2 M_\odot$ and X-ray detections that fall in the saturated regime, $\log_{10}L_X/L_{\mathrm{bol}} = -3.17^{+0.11}_{-0.16}$ (A. Núñez et al., in preparation), with uncertainties corresponding to the 16th and 84th percentiles. K2-25's X-ray flux is fully consistent with that of other young, rapidly rotating stars.

Gl 436 and GJ 3470 are field-age stars and have longer rotation periods of 44.09 days and 21.54 days, respectively (Bourrier et al. 2018b; Kosiarek et al. 2019). Veyette & Muirhead (2018) were able to constrain Gl 436's age to $8.9^{+2.3}_{-2.1}$ Gyr. Gl 436 and GJ 3470 have estimated Rossby numbers of 0.78 and 0.47, using the mass-convective turnover time relation from Wright et al. (2018) and masses from Stassun et al. (2019). These Rossby numbers are well within the unsaturated regime. K2-25 has an X-ray luminosity that is ten times larger than GJ 3470 and one hundred times larger than Gl 436, which is compatible with K2-25's youth and corresponding rapid rotation.

4.4. The XUV Spectrum

The X-ray to EUV fluxes and errors are reported in Table 4. The sum of the X-ray and EUV (XUV) irradiation that K2-25b experiences is 8763 ± 1049 erg s^{-1} cm^{-2}, where the error was calculated using the average X-ray flux uncertainty and 20% uncertainty in each EUV band. This is roughly 70% of the XUV flux estimated by Gaidos et al. (2020), who based their estimate on a scaled composite spectrum of GJ 674 and rotation-activity relations, and is consistent with their uncertainty (see their Table 1). K2-25b's XUV irradiation is roughly seven times that of Gl 436b and twice that of GJ 3470b (Bourrier et al. 2018a, 2016).

4.5. Mass-loss Rate

The mass measurement for K2-25b from Stefansson et al. (2020b) indicates its atmosphere is currently dominated by hydrogen, and is therefore still susceptible to hydrodynamic escape. We used our XUV flux to estimate the total mass-loss rate of K2-25b, adopting the energy-limited methodology as reviewed in Owen (2019). The energy-limited approach was originally derived by Watson et al. (1981) using outflow calculations for a young Earth and Venus. The equation is:

$$\dot{M} = \eta \frac{\pi R_p^3 F_{XUV}}{G M_p K_{eff}} \qquad (2)$$

$$K_{eff} = \frac{(a/R_p - 1)^2 (2a/R_p + 1)}{2(a/R_p)^3} \qquad (3)$$

where R_p is the planetary radius, F_{XUV} is the stellar XUV flux at the planet's location, and M_p is the planetary mass. This formalism assumes that K2-25b is absorbing all of the XUV flux at its optical-wavelength radius, where the energy input balances the energy necessary for escaping the planet's potential.

Two correction factors remain in Equation (2). Erkaev et al. (2007) added the K_{eff} factor (Equation (3)) to correct for the potential difference between the planet's radius and its Roche lobe, which needs to be overcome by the energetic atmosphere in order to escape. The η factor characterizes the efficiency at which the XUV radiation heats the planet's atmosphere. The exoplanet population could exhibit a wide range of heating efficiencies (0.15–0.6; Shaikhislamov et al. 2014). η has been shown to depend on the incident flux level—higher flux levels cause radiative cooling to become a limiting factor (Murray-Clay et al. 2009) –and atmospheric properties. We report our mass-loss rate in terms of η, (i.e., without assuming a heating efficiency), which enables comparison to other systems.

We calculated the total mass-loss rate to be $10.6^{+15.2}_{-6.13}\eta \times 10^{10}$ g s^{-1} assuming the planetary parameters in Table 1 and the estimated planetary mass derived from mass–radius relations. This is about 50% of the estimate from Gaidos et al. (2020), who use a different method for calculating total XUV irradiation, but agrees within our uncertainty. Stefansson et al. (2020b) used radial velocity observations from the Habitable-zone Planet Finder to measure K2-25b's mass, a challenging prospect given that the 1.8 days stellar rotation period is close to half the planetary orbital period. These authors determine a mass of $24.5^{+5.7}_{-5.2}M_\oplus$, higher than our estimate of $7M_\oplus$ and the estimate of $9.7M_\oplus$ from Gaidos et al. (2020).[10] Using their planet mass and radius gives

a mass-loss rate of $3.00^{+0.77}_{-0.71}\eta \times 10^{10}$ g s^{-1}. This is about 30% of the estimate using the parameters from Table 1 which is within our uncertainty and does not substantively alter our conclusions (see Section 5).

4.6. Photoionization Rate

The XUV irradiation of K2-25b photoionizes its exosphere. The average lifetime of an escaping neutral hydrogen atom contributes to whether or not an absorption signature should be observable in Lyα. Equation (4) gives the photoionization rate per neutral hydrogen atom given an incident flux (see e.g., Bourrier et al. 2016):

$$\Gamma_{ion} = \int_{0\,\text{Å}}^{911.8\,\text{Å}} \frac{F_{XUV}(\lambda)\sigma_{ion}(\lambda)}{hc}\lambda d\lambda \qquad (4)$$

where:

$$\begin{aligned}\sigma_{ion} &= 6.538 \times 10^{-32}\left(\frac{29.62}{\sqrt{\lambda}} + 1\right)^{-2.963} \\ &\times (\lambda - 28846.9)^2 \lambda^{2.0185}.\end{aligned} \qquad (5)$$

The photoionization rate, Γ_{ion}, is given in s^{-1}. F_{XUV} is the stellar XUV flux at the location of the planet in erg s^{-1} cm^{-2} Å^{-1}, and σ_{ion} is the photoionization cross section in cm^2 given in Equation (5) (Verner et al. 1996; Bzowski et al. 2013). The integral is over the H-ionizing portion of the electromagnetic spectrum ($\lambda \leqslant 911.8$ Å).

We calculated the photoionization rate by summing over the XUV flux values listed in Table 4 multiplied by $\sigma_{ion}(\lambda)\lambda$ evaluated at the average wavelength of each wavelength bin. This results in a photoionization rate of 9.73×10^{-5} s^{-1} at K2-25b's semimajor axis, which corresponds to a neutral hydrogen atom's lifetime of 2.86 hr. GJ 3470b was similarly found to have a short neutral hydrogen lifetime of ∼0.9 hr (Bourrier et al. 2018a). In contrast, Gl 436b has a long neutral hydrogen lifetime of about 14 hr which allows the leading and trailing regions of its exosphere to evade rapid ionization (Bourrier et al. 2016). Short neutral hydrogen lifetimes (large photoionization rates) result in smaller neutral exospheres and correspondingly shallower and shorter Lyα transits (as can be seen by comparing the Gl 436b and GJ 3470b transit signals; Bourrier et al. 2016, 2018a).

5. Discussion

Observations of young planets inform our knowledge of exoplanetary evolution, and the impact of host-star age and activity on planetary properties.

5.1. Summary

K2-25b is similar in size and proximity to its host star ($3.45R_\oplus$, 0.0288 au) to Gl 436b ($4.26R_\oplus$, 0.0287 au) and GJ 3470b ($4.57R_\oplus$, 0.0355 au). We measured K2-25's Lyα and X-ray flux and inferred the EUV flux in order to determine the planetary irradiation. Although all three planets experience EUV irradiation on the same order of magnitude, K2-25b experiences enhanced X-ray irradiation compared to the two other hot Neptunes. This is a result of K2-25's young age, and the slower decline of EUV with age compared to X-rays (Peacock et al. 2020). The large XUV irradiation results in an estimated maximum mass-loss rate ($10.6^{+15.2}_{-6.13}\eta \times 10^{10}$ g s^{-1})

---

[10] They also combined K2 and ground-based photometry observations to obtain a planetary radius of $3.44 \pm 0.12R_\oplus$, in agreement with the value from Thao et al. (2020) and quoted in Table 1.

that is five times larger than for Gl 436b ($2.20\eta \times 10^{10}$ g s^{-1}; Bourrier et al. 2016). The larger mass-loss rate for K2-25b means that if the same atmospheric escape process translates across all three planets, then we should be able to observe an escaping neutral hydrogen exosphere surrounding K2-25b.

Our analysis of two HST/STIS observations of K2-25 in Lyα yielded a nondetection of an extended neutral hydrogen envelope around K2-25b despite the large mass-loss rate. This suggests that K2-25b is either not experiencing significant atmospheric escape, or other factors result in mass loss that is unobservable in our Lyα observations. The latter could be due to properties of the system itself. While adopting the $24.5 M_\oplus$ mass in place of the value from mass–radius relations results in a factor of three lower mass-loss rate, this reduction is not sufficient to imply a nondetection of an evaporating atmosphere, and we therefore explore the latter possibility.

5.2. Astrophysical Causes for a Nondetection

A possible explanation for the suppression of a neutral hydrogen exosphere is a denser, non-hydrogen-dominated atmosphere. A higher mean molecular weight would decrease the atmospheric scale height, reducing the likelihood of hydrodynamic escape. This could be possible if K2-25b lost its primordial atmosphere when it was younger, which would be consistent with the potentially short $\sim$100 Myr timescale of photo evaporation and inconsistent with the longer Gyr timescale proposed by King & Wheatley (2021). García Muñoz et al. (2020) suggest a transition around $\rho_p \sim$ 2–3 g cm^{-3}: planets with bulk densities below 2 g cm^{-3} have neutral hydrogen-dominated atmospheres that allow the detection of an extended atmosphere in Lyα. Planets with bulk densities above 3 g cm^{-3} could have atmospheres dominated by heavier species, resulting in no detection of atmospheric absorption in Lyα regardless of mass-loss rate. With the planetary mass estimate based on mass–radius relations ($7^{+10}_{-4} M_\oplus$), K2-25b has a bulk density ($\rho_p = 0.94^{+1.35}_{-0.54}$ g cm^{-3}) that places it within the regime of H-dominated atmospheres that should result in Lyα absorption if the atmosphere is escaping. However, the measurement from Stefansson et al. (2020b) results in a bulk density that agrees with either a H-dominated or water-dominated atmosphere ($\rho_p = 3.28 \pm 0.8$ g cm^{-3}). In the framework of García Muñoz et al. (2020), K2-25b could potentially then fall into the regime where planets typically do not exhibit Lyα absorption even with high mass-loss rates.

K2-25's youth could also impact the detectability of the planet's Lyα transit. The estimated lifetime before ionization of an escaping neutral hydrogen atom in K2-25b's exosphere is short (2.86 hr) compared to Gl 436b ($\sim$12 hr). The short lifetime could indicate that enough neutral atoms are ionized before they are able to travel far enough to form a large neutral hydrogen exosphere. The result may be a smaller exosphere more similar to that of GJ 3470. Our observational strategy was set prior to the detection of GJ 3470, and was optimized for the detection of a more extended exosphere.

The exosphere could be interacting with high-velocity stellar winds from its host (e.g., Bourrier & Lecavelier des Etangs 2013; Kislyakova et al. 2014; Cohen et al. 2015). Via charge exchange, fast-traveling protons from the stellar wind may receive an electron from the neutral hydrogen in the transiting planet's atmosphere, suffering little deflection or change in

kinetic energy from the collision. Therefore, if the stellar wind is high-speed, the now-neutral stellar wind could result in Lyα absorption beyond the Lyα emission feature–where, for K2-25, there is little signal (cf. Bourrier et al. 2016).

Carolan et al. (2021) explored the effects of varying stellar wind strengths on the Lyα transits of close-in planets with 3D hydrodynamic simulations (see also Carolan et al. 2020 and Vidotto & Cleary 2020). They showed that stellar winds provide an external pressure that can confine the atmosphere of an exoplanet and decrease the exosphere's transit depth by a factor of about two. We make a rough estimate of the stellar mass-loss rate for K2-25 using its X-ray flux (3.17×10^6 erg s^{-1} cm^{-2}) and the observed relationship between X-ray flux and the mass-loss rates of main-sequence stars (Wood et al. 2005, c.f. Figure 3). This gives $\sim 0.8 \dot{M}_\odot$. When making this estimate, we assume that the mass-loss rate per unit surface area reaches an asymptote at $\sim 9 \dot{M}_\odot / A_\odot$ (units of solar mass-loss rate per solar-surface area) for X-ray fluxes greater than 10^6 erg s^{-1} cm^{-2}. The inferred mass-loss rate for K2-25 is significantly lower than the wind strengths from Carolan et al. (2021) and so we do not a priori expect that the wind would inhibit the detection of an escaping exosphere. Our stellar mass-loss estimate is highly uncertain, however, as there are no observational constraints on K2-25's stellar wind strength and current $\dot{M}_\star \propto F_X$ relations do not extend to the high X-ray fluxes exhibited by young M dwarfs.

The stellar and planetary properties that concern the properties of evaporating atmospheres are far from clear, and K2-25b is currently the only young Neptune in the literature with an analysis of its Lyα transit. Our nondetection of an extended atmosphere is inconsistent with the extended, cometary tail seen around Gl 436b, but permits the presence of smaller exospheres more similar to that of GJ 3470b. We considered the scenario where we obtained a total of 3 HST visits similar in quality to our Visit 2. We can only detect an exosphere of >0.5 R$_\star$ in the Lyα blue wing, which does not enable us to probe atmospheres as small as could be expected. K2-25b needs further modeling to learn about the expected size and shape of a potential exosphere, which could then guide future observations.

Facilities: HST/STIS, XMM-Newton.

Software: astropy (Price-Whelan et al. 2018), batman (Kreidberg 2015), calstis (https://github.com/spacetelescope/stistools), emcee (France et al. 2013), lyapy (Youngblood et al. 2016), matplotlib (Hunter 2007), numpy (Harris et al. 2020), scipy (Virtanen et al. 2020).

ORCID iDs

Keighley E. Rockcliffe ⓞ https://orcid.org/0000-0003-1337-723X
Elisabeth R. Newton ⓞ https://orcid.org/0000-0003-4150-841X
Allison Youngblood ⓞ https://orcid.org/0000-0002-1176-3391
Vincent Bourrier ⓞ https://orcid.org/0000-0002-9148-034X
Andrew W. Mann ⓞ https://orcid.org/0000-0003-3654-1602
Zachory Berta-Thompson ⓞ https://orcid.org/0000-0002-3321-4924
Marcel A. Agüeros ⓞ https://orcid.org/0000-0001-7077-3664
Alejandro Núñez ⓞ https://orcid.org/0000-0002-8047-1982
David Charbonneau ⓞ https://orcid.org/0000-0002-9003-484X

References

Beaugé, C., & Nesvorný, D. 2013, ApJ, 763, 12
Ben-Jaffel, L., & Sona Hosseini, S. 2010, ApJ, 709, 1284
Bourrier, V., Ehrenreich, D., & Lecavelier des Etangs, A. 2015, A&A, 582, A65
Bourrier, V., & Lecavelier des Etangs, A. 2013, A&A, 557, A124
Bourrier, V., Lecavelier des Etangs, A., Dupuy, H., et al. 2013, A&A, 551, A63
Bourrier, V., Lecavelier des Etangs, A., Ehrenreich, D., et al. 2018a, A&A, 620, A147
Bourrier, V., Lecavelier des Etangs, A., Ehrenreich, D., Tanaka, Y. A., & Vidotto, A. A. 2016, A&A, 591, A121
Bourrier, V., Lovis, C., Beust, H., et al. 2018b, Natur, 553, 477
Bowers, C. W. 1997, in HST Calibration Workshop with a New Generation of Instruments, ed. S. Casertano et al. (Baltimore, MD: Space Telescope Science Institute), 18
Brown, T. M., Charbonneau, D., Gilliland, R. L., Noyes, R. W., & Burrows, A. 2001, ApJ, 552, 699
Bzowski, M., Sokół, J. M., Tokumaru, M., et al. 2013, Solar Parameters for Modeling the Interplanetary Background, Vol. 13 (New York: Springer), 67
Carolan, S., Vidotto, A. A., D'Angelo, C. V., & Hazra, G. 2020, MNRAS, 498, L53
Carolan, S., Vidotto, A. A., Plavchan, P., Villarreal D'Angelo, C., & Hazra, G. 2020, MNRAS, 498, L53

Carolan, S., Vidotto, A. A., Villarreal D'Angelo, C., & Hazra, G. 2021, MNRAS, 500, 3382
Cohen, O., Ma, Y., Drake, J. J., et al. 2015, ApJ, 806, 41
Davis, T. A., & Wheatley, P. J. 2009, MNRAS, 396, 1012
Debrecht, A., Carroll-Nellenback, J., Frank, A., et al. 2020, MNRAS, 493, 1292
dos Santos, L. A., Ehrenreich, D., Bourrier, V., et al. 2019, A&A, 629, A47
Douglas, S. T., Curtis, J. L., Agüeros, M. A., et al. 2019, ApJ, 879, 100
Ehrenreich, D., Bourrier, V., Wheatley, P. J., et al. 2015, Natur, 522, 459
Erkaev, N. V., Kulikov, Y. N., Lammer, H., et al. 2007, A&A, 472, 329
Fontenla, J. M., Landi, E., Snow, M., & Woods, T. 2014, SoPh, 289, 515
Foreman-Mackey, D., Hogg, D. W., Lang, D., & Goodman, J. 2013, PASP, 125, 306
France, K., Froning, C. S., Linsky, J. L., et al. 2013, ApJ, 763, 149
Fulton, B. J., & Petigura, E. A. 2018, AJ, 156, 264
Fulton, B. J., Petigura, E. A., Howard, A. W., et al. 2017, AJ, 154, 109
Gaidos, E., Hirano, T., Wilson, D. J., et al. 2020, MNRAS, 498, L119
García Muñoz, A., Youngblood, A., Fossati, L., et al. 2020, ApJL, 888, L21
Gehrels, N. 1986, ApJ, 303, 336
Ginzburg, S., Schlichting, H. E., & Sari, R. 2018, MNRAS, 476, 759
Gossage, S., Conroy, C., Dotter, A., et al. 2018, ApJ, 863, 67
Harris, C. R., Millman, K. J., van der Walt, S. J., et al. 2020, Natur, 585, 357
Harris, D. L., III 1948, ApJ, 108, 112
Hébrard, G., & Moos, H. W. 2003, ApJ, 599, 297
Holmström, M., Ekenbäck, A., Selsis, F., et al. 2008, Natur, 451, 970
Huitson, C. M., Sing, D. K., Vidal-Madjar, A., et al. 2012, MNRAS, 422, 2477
Hunter, J. D. 2007, Computing in science & engineering, 9, 90
Jin, S., Mordasini, C., Parmentier, V., et al. 2014, ApJ, 795, 65
Kain, I. J., Newton, E. R., Dittmann, J. A., et al. 2020, AJ, 159, 83
Kanodia, S., Wolfgang, A., Stefansson, G. K., Ning, B., & Mahadevan, S. 2019, MRExo: Non-parametric Mass-radius Relationship for Exoplanets, Astrophysics Source Code Library, ascl:1912.020
King, G. W., & Wheatley, P. J. 2021, MNRAS, 501, L28
Kislyakova, K. G., Johnstone, C. P., Odert, P., et al. 2014, A&A, 562, A116
Kosiarek, M. R., Crossfield, I. J. M., Hardegree-Ullman, K. K., et al. 2019, AJ, 157, 97
Kreidberg, L. 2015, PASP, 127, 1161
Kulow, J. R., France, K., Linsky, J., & Loyd, R. O. P. 2014, ApJ, 786, 132
Kurokawa, H., & Nakamoto, T. 2014, ApJ, 783, 54
Lammer, H., Selsis, F., Ribas, I., et al. 2003, ApJL, 598, L121
Lavie, B., Ehrenreich, D., Bourrier, V., et al. 2017, A&A, 605, L7
Lecavelier Des Etangs, A. 2007, A&A, 461, 1185
Lee, E. J., & Connors, N. J. 2021, ApJ, 908, 32
Linsky, J. L., Draine, B. T., Moos, H. W., et al. 2006, ApJ, 647, 1106
Linsky, J. L., Fontenla, J., & France, K. 2014, ApJ, 780, 61
Lopez, E. D., & Fortney, J. J. 2013, ApJ, 776, 2
Loyd, R. O. P., France, K., Youngblood, A., et al. 2018, ApJ, 867, 71
Lundkvist, M. S., Kjeldsen, H., Albrecht, S., et al. 2016, NatCo, 7, 11201
Mann, A. W., Gaidos, E., Mace, G. N., et al. 2016, ApJ, 818, 46
Mazeh, T., Holczer, T., & Faigler, S. 2016, A&A, 589, A75
McCann, J., Murray-Clay, R. A., Kratter, K., & Krumholz, M. R. 2019, ApJ, 873, 89
Murray-Clay, R. A., Chiang, E. I., & Murray, N. 2009, ApJ, 693, 23
Ning, B., Wolfgang, A., & Ghosh, S. 2018, ApJ, 869, 5
Owen, J. E. 2019, AREPS, 47, 67
Owen, J. E., & Jackson, A. P. 2012, MNRAS, 425, 2931
Owen, J. E., & Lai, D. 2018, MNRAS, 479, 5012
Owen, J. E., & Wu, Y. 2013, ApJ, 775, 105
Owen, J. E., & Wu, Y. 2017, ApJ, 847, 29
Peacock, S., Barman, T., Shkolnik, E. L., et al. 2019, ApJ, 886, 77
Peacock, S., Barman, T., Shkolnik, E. L., et al. 2020, ApJ, 895, 5
Price-Whelan, A. M., Sipőcz, B. M., Günther, H. M., et al. 2018, AJ, 156, 123
Redfield, S., & Linsky, J. L. 2000, ApJ, 534, 825
Redfield, S., & Linsky, J. L. 2008, ApJ, 673, 283
Shaikhislamov, I. F., Khodachenko, M. L., Sasunov, Y. L., et al. 2014, ApJ, 795, 132
Sing, D. K., Vidal-Madjar, A., Désert, J. M., Lecavelier des Etangs, A., & Ballester, G. 2008, ApJ, 686, 658
Stassun, K. G., Oelkers, R. J., Paegert, M., et al. 2019, AJ, 158, 138
Stefansson, G., Mahadevan, S., Maney, M., et al. 2020a, AJ, 160, 192
Stefansson, G., Mahadevan, S., Maney, M., et al. 2020b, AJ, 160, 192
Szabó, G. M., & Kiss, L. L. 2011, ApJL, 727, L44
Thao, P. C., Mann, A. W., Johnson, M. C., et al. 2020, AJ, 159, 32
Tremblin, P., & Chiang, E. 2013, MNRAS, 428, 2565

Verner, D. A., Ferland, G. J., Korista, K. T., & Yakovlev, D. G. 1996, ApJ, 465, 487

Veyette, M. J., & Muirhead, P. S. 2018, ApJ, 863, 166

Vidotto, A. A., & Cleary, A. 2020, MNRAS, 494, 2417

Villarreal D'Angelo, C., Esquivel, A., Schneiter, M., & Sgró, M. A. 2018, MNRAS, 479, 3115

Virtanen, P., Gommers, R., Oliphant, T. E., et al. 2020, NatMe, 17, 261

Watson, A. J., Donahue, T. M., & Walker, J. C. G. 1981, Icar, 48, 150

Wood, B. E., Linsky, J. L., Hébrard, G., et al. 2004, ApJ, 609, 838

Wood, B. E., Müller, H. R., Zank, G. P., Linsky, J. L., & Redfield, S. 2005, ApJL, 628, L143

Wright, N. J., Newton, E. R., Williams, P. K. G., Drake, J. J., & Yadav, R. K. 2018, MNRAS, 479, 2351

Yelle, R. V. 2004, Icar, 170, 167

Youngblood, A., France, K., Loyd, R. O. P., et al. 2016, ApJ, 824, 101